Onset of density-driven instabilities in fractured aquifers

Seyed Mostafa Jafari Raad and Hassan Hassanzadeh[*]

Department of Chemical and Petroleum Engineering, Schulich School of Engineering, University of Calgary,
2500 University Drive NW, Calgary, Alberta, Canada T2N 1N4

Linear stability analysis is conducted to study the onset of density-driven convection involved in solubility trapping of CO_2 in fractured aquifers. The effect of physical properties of a fracture network on the stability of a diffusive boundary layer in a saturated fractured porous media is investigated using the dual porosity concept. Linear stability analysis results show that both fracture interporosity flow and fracture storativity play an important role in the stability behavior of the system. It is shown that a diffusive boundary layer under the gravity field in fractured porous media with lower fracture storativity and/or higher fracture interporosity flow coefficient is more stable. We present scaling relations for the onset of convective instability in fractured aquifers with single and variable matrix block size distribution. These findings improve our understanding of density-driven flow in fractured aquifers and are important in the estimation of potential storage capacity, risk assessment, and storage site characterization and screening.

I. INTRODUCTION

Density-driven convection in porous media is of great importance for a wide range of applications related to groundwater, soil contamination, formation of ore deposits, carbon dioxide (CO_2) sequestration, and petroleum and geothermal reservoirs [1–4]. Natural convection can develop due to an unstable density profile in the gravity field, which can be attributed to either temperature or concentration gradient. Conceptual basis and general importance of both solutal and thermal density-driven convection in porous media have been comprehensively addressed in previous studies [5–7]. The conditions under which density-driven convection develops in the concentration field have received great attention in the past decade. Density-driven convection involved in geological sequestration of CO_2 in deep saline aquifers is a good example of the current interest [8–10]. Geological sequestration of CO_2 has been proposed as a short-term implementable option to reduce anthropogenic CO_2 emissions from the atmosphere [11]. Deep saline aquifers with their high storage capacity and worldwide accessibility have been identified as the best alternative for CO_2 storage [11]. Once CO_2 is injected into an aquifer it migrates upwards due to its buoyancy and spreads at the top of aquifers below a low-permeability cap rock from where it gradually dissolves into the underlying brine [1]. While most dissolved gases decrease fluid density, dissolution of CO_2 into brine slightly increases the density of the brine phase. The CO_2-rich brine phase sinks down due to gravitational instabilities that drive the convective dissolution. Convective dissolution enhances the mass transfer of CO_2 from the CO_2 free phase (plume) to the underlying brines. This process significantly decreases the volume of free-phase CO_2 under the cap rock, and consequently reduces risk of

CO_2 leakage [12,13]. The onset of density-driven convection in porous media, in the context of the CO_2 sequestration process, has been the subject of several studies as it impacts the long-term storage security. The onset of density-driven convection has been often studied using linear stability theory and energy method in both isotropic [14–17] and anisotropic [18–21] porous media. This problem has been also addressed by a number of numerical studies [22–26]. These studies enhanced the understanding of the density-driven convection in the context of CO_2 sequestration in deep saline aquifers. However, previous studies have been focused on CO_2 storage in nonfractured (single-porosity) deep saline aquifers.

Understanding the density-driven convection involved in dissolution of CO_2 in fractured formations is important since fractured aquifers are widespread and are gaining importance for their potential to host captured CO_2 for storage. Density-driven convection in fractured porous media has been the subject of several studies mostly related to geothermal energy, fractured petroleum reservoir exploration, hazardous waste disposal, formation of ore deposits, and groundwater applications. The onset of density-driven instabilities in fractured aquifers with a transient base state in the context of geological storage of CO_2 has not been studied sufficiently.

In the early studies on density-driven convection in fractured porous media, a single-fracture medium was approximated by a three-dimensional (3D) fluid-filled vertical slab or vertically oriented saturated porous box heated from below. This configuration was used for cases with either impermeable and nonconducting [27] or impermeable conducting fracture walls [28–32]. Later, more complex models were considered to study this phenomenon either within a single fracture [30,33–39] or in a fracture network [40–46] under various boundary conditions. Through these studies, it was shown that the density-driven flow within a single fracture with nonconducting walls is mostly governed by the stability criteria similar to those reported for stability of a diffusive boundary

---

[*]hhassanz@ucalgary.ca

layer in a vertically saturated porous medium [27,47,48]. It was reported that conducting fracture walls have a stabilizing effect on density-driven convection within the fracture [3,28–30]. The stabilizing effect of conducting fracture walls is less distinct when the adjacent matrix blocks contribute to the transport process as compared to the cases when the fracture wall acts as a boundary [3,30,31,49,50].

The stability of density-driven convection and the associated convective flow in fracture networks have been often studied using direct numerical simulations. Findings from previous studies show that fracture geometry and hydraulic properties play an important role in the stability of density-driven convection and the convective flow pattern within the fractured system. It has been observed that low fracture aperture, low matrix permeability, and high matrix porosity impede density-driven convection within the fracture network with orthogonal continuous or/and inclined discontinuous fractures [41,43]. It was shown that the likelihood of continuous fracture circuits and thus the strength of density-driven convection in a fracture network increase as the fracture density and fracture length increase [42,44,51].

Although significant achievements were made in the study of density-driven flow within fractured porous media, stability analysis of density-driven flows with transient temperature (or concentration) field in a fractured porous medium has not been studied sufficiently. The objectives of this study are to perform linear stability analysis of transient single-phase flow and transport in fractured rocks and develop scaling relations that relate the onset of density-driven instabilities to the key physical properties of the fractured rocks.

The common approach to study the stability of fluids in porous media is to use linear stability analysis. This approach is well accepted and has been widely used in the literature [9,52–54]. In addition, we use the well-known dual porosity idealization of fractured porous media pioneered by Barenblatt *et al.* [55], Warren and Root [56], and Odeh [57] to model single-phase flow in fractured media. The applicability of this elegant approach to model single-phase flow and transport in fractured porous media has been well accepted in the literature. However, while the dual porosity approach works very well for the single-phase flow situations, which is the subject of our study, it has some essential deficiencies when multiple phases are present. For instance, the gravity drainage process, capillarity, and reinfiltration phenomena are not easy to describe using the dual porosity approach. In this work, we deal with single-phase flow and transport of CO_2-saturated brine and therefore gravity drainage process, capillarity, and reinfiltration phenomena are not involved.

Based on the dual porosity concept, which is believed to be appropriate for single-phase flow and transport in fractured rocks, fractured porous systems are considered to be composed of two media, fracture networks with high permeability and low storativity and rock matrix blocks with low permeability and high storativity [46,55,56]. In this model, fractures with high permeability contribute to the main flow path for fluid in the fractured porous medium and matrix blocks act as sink or source. Thus, it is expected that density-driven flow develops in the brine-filled fracture networks. However, diffusive solute transport and hence density-driven flow within a fracture is strongly coupled with mass transfer in matrix blocks through the fracture-matrix interaction. The contrast between the dissolved CO_2 concentration in fractures and adjacent matrix blocks leads to mass transfer between matrix and fracture. Dissolved CO_2 mass transfer from the fracture to the matrix block can act as a sink for the accumulated CO_2 in the fissures [58] and consequently affect the stability behavior of the diffusive boundary layer developed in the fracture network.

Determination of the effect of the physical properties of the fractured porous media on the stability of a diffusive boundary layer requires a coupled model that takes into account the transient solute transport between the fracture and matrix blocks.

In this work, we performed linear stability analysis to study the instability behavior of a gravitationally unstable diffusive boundary layer associated with dissolution of CO_2 in a saturated fractured porous medium. The effect of fracture physical properties and also fracture-matrix interaction on the instability behavior of a diffusive boundary layer within the fractured porous medium was investigated. Scaling relationships that can be used to estimate the onset of density-driven instabilities were reported as a function of the most common physical properties of the fractured porous media.

II. MODEL DESCRIPTION AND GOVERNING EQUATIONS

An idealized picture of fractured rock is shown in Fig. 1(a). We consider a two-dimensional (2D) fractured aquifer of thickness H with slab-shape matrix blocks saturated with quiescent brine as shown in Fig. 1(b). No-flow boundary conditions are considered at the top and bottom of the domain. At the lower boundary, mass flux is set to zero, while constant concentration of CO_2 species is set at the top of the domain with respect to the mass transfer. Assuming single-phase flow and consequently in the absence of capillarity, the interface between CO_2 and water is considered sharp with a constant concentration of dissolved CO_2 [15].

To study the problem, the coupled mass transfer between the fracture and matrix blocks is treated using the dual porosity model concept [56]. Based on this, the matrix blocks act as a sink for the fracture network.

Using the Boussinesq approximation and in the absence of fluid compressibility, viscosity variation, and dispersion, the governing equations of nonreactive single-phase flow and transport in a fracture domain under the dual porosity concept can be written as follows:

$$\phi_f D_f (\nabla^2 C_f) - \vec{\mathbf{v}} . \nabla C_f$$

$$= \phi_f \frac{\partial C_f}{\partial t} + \int_{L_{c\min}}^{L_{c\max}} Q(L_c) J(L_c) dL_c, \qquad (1)$$

$$\nabla \cdot \vec{\mathbf{v}} = 0, \qquad (2)$$

$$\vec{\mathbf{v}} = -\frac{k}{\mu}(\nabla p - \rho \mathbf{g}), \qquad (3)$$

$$\phi_m D_m \frac{\partial^2 C_m}{\partial \ell^2} = \phi_m \frac{\partial C_m}{\partial t}, \qquad (4)$$

where $\mathbf{v}(u,w)$ is the vector of Darcy velocity, p is the pressure, ℓ denotes the spatial coordinate in the matrix block domain
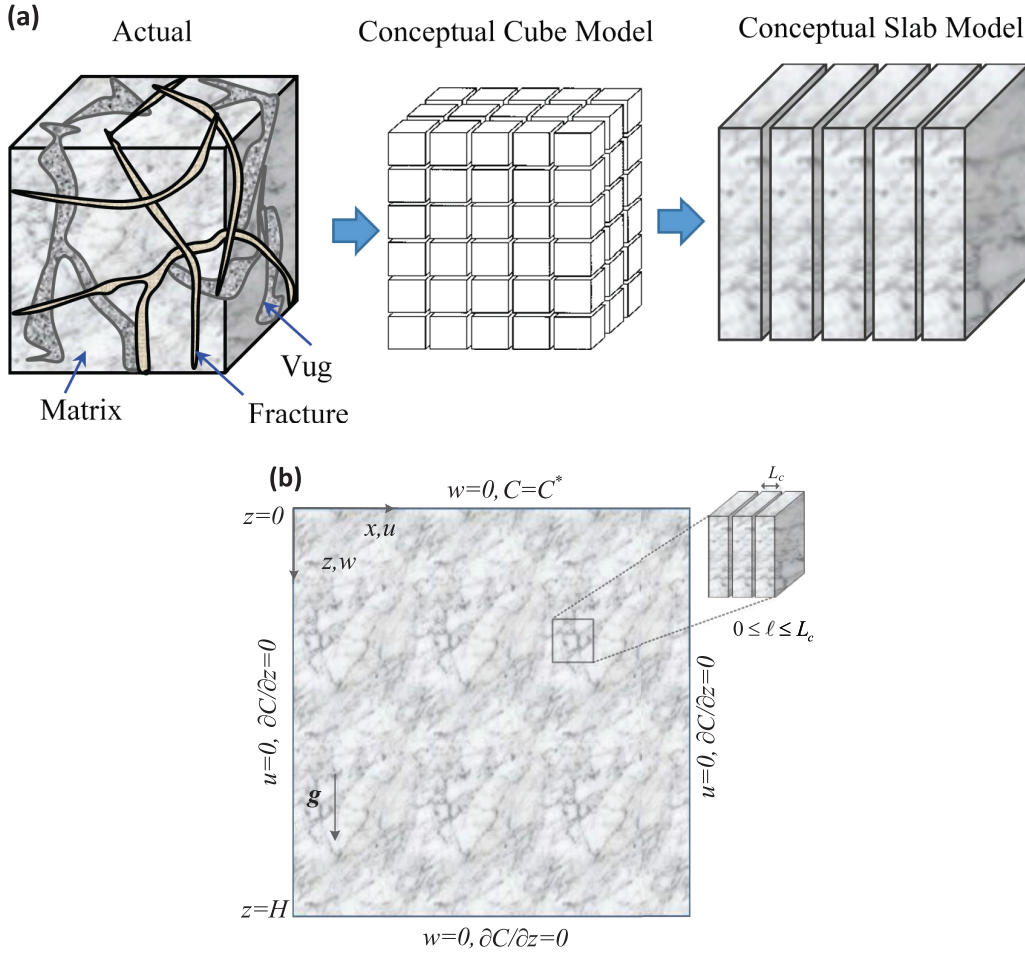
(a)

(b)

FIG. 1. (a) Idealization of fractured rock with single-size block matrix and (b) geometry and boundary conditions considered in this study [56]. C^* is the equilibrium concentration, and C is the concentration of the diffusing species in the aqueous phase. u and w denote the horizontal and vertical components of the Darcy velocity in the fracture domain, respectively.

with $0 \leqslant \ell \leqslant L_c$, and L_c is the characteristic thickness of the matrix block. $C_f(x,z,t)$ and $C_m(\ell,t)$ are the concentrations of CO_2 in fracture and matrix, respectively; μ is the viscosity; k is the permeability; ϕ is the porosity; and $\mathbf{g}$ is the gravitational acceleration. D is the effective molecular diffusion coefficient and is assumed to be independent of concentration for dilute solutions. Subscripts m and f stand for matrix and fracture, respectively. ρ is the brine density defined as $\rho = \rho_b(1 + \beta C)$ where ρ_b is the density of fresh brine, β is the coefficient of density variation with concentration, and C is the concentration of dissolved CO_2 in water. The integral term (or sink) in Eq. (1) accounts for the mass transfer of dissolved CO_2 between matrix blocks and the fractures, and $L_{c\min}$ and $L_{c\max}$ are minimum and maximum matrix block sizes, respectively.

$Q(L)$ is the rate of mass transfer from the fracture to the adjacent matrix blocks. For a matrix block with slab-shape geometry the rate of mass transfer from the fracture to the adjacent matrix block is expressed as

$$Q(L_c) = \frac{\phi_m D_m}{L_c} \left. \frac{\partial C_m}{\partial \ell} \right|_{\ell = L_c}. \qquad (5)$$

Function $J(L)$ in Eq. (1) is the probability density function (PDF) describing the size distribution function for the matrix blocks. For a fractured porous medium with a single-size

matrix block of thickness L_c the sink term in Eq. (1) is reduced to $Q(L_c)$.

A fractured porous medium may be classified as an intensely or sparsely fractured system depending on the skewness of the block length probability density function (PDF) [59]. Linear and exponential probability density functions are the two most common continuous block size distributions used in the modeling of dual porosity media [60]. In this study, we use exponential probability density as the most general function to characterize the matrix block size distribution. The corresponding function for an exponential block size distribution is given by [61]

$$J(L_c) = \frac{m e^{-mL_c}}{m e^{-mL_{c\min}} - m e^{-mL_{c\max}}}, \qquad (6)$$

where m is an exponential distribution constant; $L_{c\min}$ and $L_{c\max}$ are minimum and maximum matrix block sizes existing in the distribution, respectively.

It has been observed that a collection of continuous matrix blocks with different characteristic lengths can be interpreted using a single-matrix block with an equivalent length [62], where the equivalent length is obtained based on the matrix block size distribution.

In other words, the sink term in fracture conservation mass Eq. (1) is equivalent to the fracture interporosity flow with an equivalent length L_{ce} as given by

$$\int_{L_{c\min}}^{L_{c\max}} Q(L_c)J(L_c)dL_c \cong \frac{\phi_m D_m}{L_{ce}} \frac{\partial C_m}{\partial \ell}\bigg|_{\ell=L_{ce}}. \quad (7)$$

In the following, the above formulation is used to perform the linear stability analysis.

III. BASE-STATE SOLUTION

At the early times and prior to the onset of convection, molecular diffusion is the dominant mechanism involved in transport of dissolved CO_2. In this case, the dimensionless equations governing the mass transfer within the fractured porous media can be written as follows:

$$\frac{\partial^2 \hat{C}_{0f}}{\partial \hat{z}^2} - \frac{\lambda}{\hat{L}_e}\frac{1-\omega}{\omega}\frac{\partial \hat{C}_{0m}}{\partial \hat{\ell}}\bigg|_{\hat{\ell}=\hat{L}_e} = \frac{\partial \hat{C}_{0f}}{\partial \hat{t}}, \quad (8)$$

$$\frac{\partial^2 \hat{C}_{0m}}{\partial \hat{\ell}^2} = \frac{1}{\lambda}\frac{\partial \hat{C}_{0m}}{\partial \hat{t}}, \quad (9)$$

where subscript 0 stands for the base state. We use $H, L_{c\max}$, C^*, and H^2/D_f to scale the spatial coordinates in the fracture domain (x, z), the spatial coordinate in the matrix block domain (ℓ), concentration, and time, respectively. Using these scalings the governing equations are nondimensionalized. In the above equations $\omega = \phi_f/\phi_t$ is the storativity, $\lambda = D_m H^2/D_f L_{c\max}^2$ is the interporosity flow coefficient, and $\hat{L}_e = L_{ce}/L_{c\max}$ is the dimensionless matrix block equivalent thickness. The storativity coefficient, $\omega = \phi_f/\phi_t$, is defined as the pore volume of the fracture per total pore volume of the fractured porous medium where subscripts f and t refer to the fracture

and the total system (both fracture and matrix domains), respectively.

In the case of exponential distribution, the equivalent thickness in dimensionless form is expressed as [63]

$$\hat{L}_e = \frac{(\alpha F_h + 1)e^{-\alpha F_h} - (\alpha + 1)e^{-\alpha}}{\alpha(e^{-\alpha F_h} - e^{-\alpha})}, \quad (10)$$

where $F_h = L_{c\min}/L_{c\max}$, and α is a dimensionless exponential distribution constant.

The following initial and boundary conditions are used to close the formulation.

For fracture: $\hat{C}_{0f}(\hat{z}, \hat{t}=0) = 0$, $\hat{C}_{0f}(0, \hat{t}) = 1$,

$$\text{and } \partial \hat{C}_{0f}(0,\hat{t})/\partial \hat{z} = 0. \quad (11)$$

For matrix: $\hat{C}_{0m}(\hat{\ell}, \hat{t}=0) = 0$, $\hat{C}_{0m}(\hat{L}_e, \hat{t}) = \hat{C}_{0f}$,

$$\text{and } \partial \hat{C}_{0m}(0,\hat{t})/\partial \hat{\ell} = 0. \quad (12)$$

The base-state solution for the concentration field in the fracture domain can be obtained by using the Laplace transform and inverted to the time domain using residue theorem [64] as given by

$$\hat{C}_{0f}(\hat{z}, \hat{t}) = 1 + \sum_{n=1}^{\infty} (-1)^{n+1} \frac{(2n-1)\pi}{\eta f'}$$

$$\times \cos\left[\frac{(2n-1)\pi}{2}(1-\hat{z})\right] \exp(\eta_n \hat{t}), \quad (13)$$

where

$$f(\eta_n) = \eta_n + \frac{\lambda}{\hat{L}_e}\frac{1-\omega}{\omega}\sqrt{\frac{\eta_n}{\lambda}}\tanh\left(\sqrt{\frac{\eta_n}{\lambda}}\hat{L}_e\right), \quad (14)$$
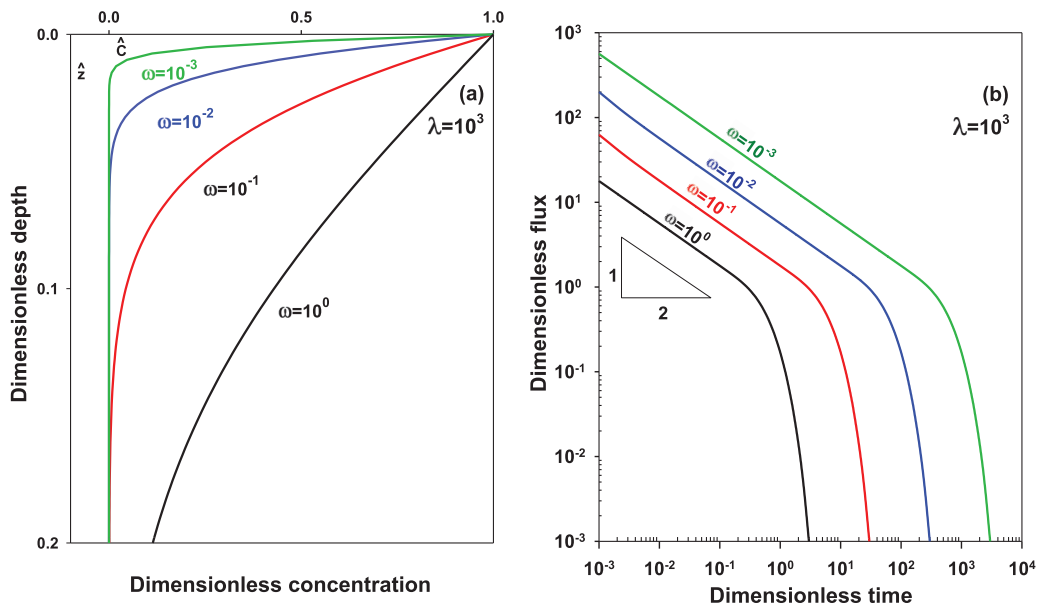

FIG. 2. (a) Base-state concentration profiles versus depth at $\hat{t} = 0.08$ and (b) CO_2 diffusive flux at the upper interface for fracture domain with a constant fracture interporosity flow coefficient of $\lambda = 10^3$ and different fracture storativity coefficients $\omega = 1$, $\omega = 10^{-1}$, $\omega = 10^{-2}$, and $\omega = 10^{-3}$.
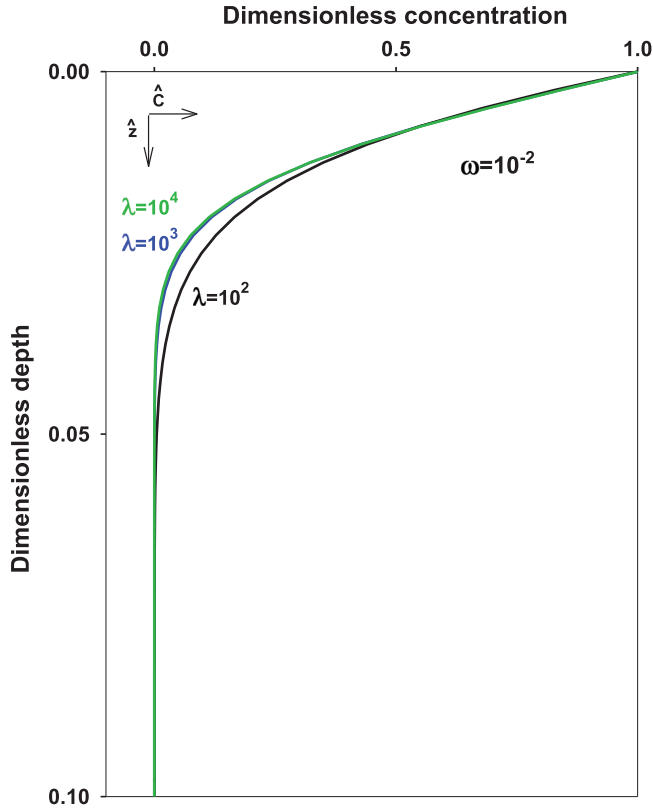
FIG. 3. Base-state concentration profiles versus depth in fracture domain with fracture storativity $\omega = 10^{-2}$, and different fracture interporosity flow coefficients of $\lambda = 10^2$, 10^3, and 10^4 at $\hat{t} = 0.08$.

and $f' = df(\eta_n)/d\eta_n$ and η_n are roots of the following non-linear equation:

$$f(\eta_n) + \frac{(2n-1)^2\pi^2}{4} = 0. \tag{15}$$

Figure 2(a) shows the base-state concentration profiles versus depth in the fracture domain with different fracture storativity coefficients (ω) and constant fracture interporosity flow coefficient (λ) at a given time ($\hat{t} = 0.08$). It can be observed that diffusive mass transfer of CO_2 in a fracture is much slower when the fracture storativity decreases. This is due to the fact that the matrix blocks act as a sink for the dissolved CO_2. Note that $\omega = 1$ denotes the single-porosity system with properties of the fracture domain. A low storativity implies larger matrix pore volume per unit bulk volume of the fractured media and hence a much stronger sink for the dissolved CO_2.

Figure 2(b) shows the time-dependent diffusive flux at the upper interface ($z = 0$). The results for diffusive flux versus time clearly indicate that the flux of CO_2 at the interface into the domain is higher for a system with lower fracture storativity during the early time and later throughout the shutdown period when the effect of concentration reaches the bottom boundary.

Figure 3 shows the dependency of the base-state concentration profile on the fracture interporosity flow coefficient. It can be observed that increase of the fracture interporosity flow coefficient at a constant fracture storativity retards the propagation of CO_2 concentration in the fracture domain. Solution of the base-state concentration also shows that for a fractured porous medium with fracture interporosity flow coefficients larger than $\lambda > 10^3$, the concentration within the fracture domain is less sensitive to the fracture interporosity flow coefficient. Later, we will show how the dependency of the concentration profile on the physical properties of the system may impact the onset of density-driven instabilities.

IV. LINEAR STABILITY ANALYSIS

The linear stability analysis determines the time at which the diffusive boundary layer becomes unstable leading to convective mixing of CO_2. As it was discussed earlier, convective mixing plays an important role in the rate of CO_2 solubility trapping. We performed the linear stability analysis under
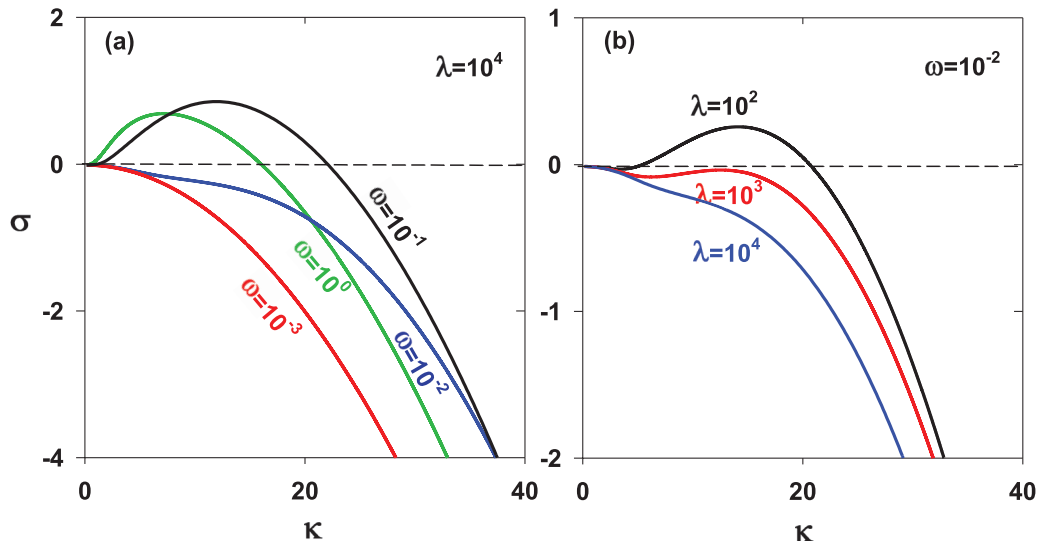

FIG. 4. Perturbation growth rates versus wave number for systems with different fracture storativity and interporosity flow coefficients at a constant $Ra = 500$ and $\hat{t}_0 = 18 \times 10^{-3}$.
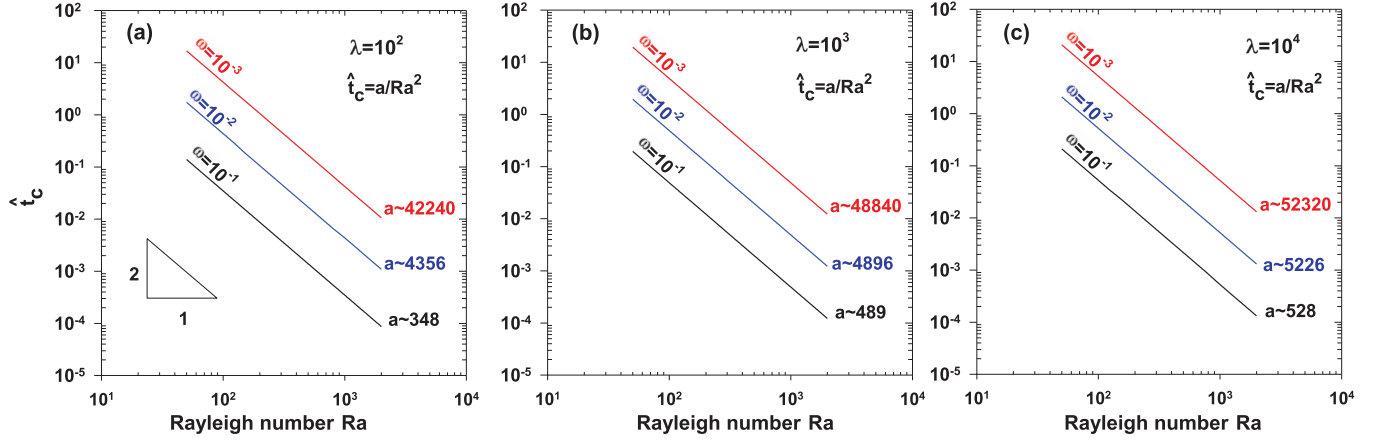
FIG. 5. Onset of instability scaled with Ra for fractured systems with single-size matrix blocks at different fracture storativity and interporosity flow coefficients.

quasi-steady-state approximation (QSSA) [52] to study the growth of instabilities of a diffusive boundary layer involved in CO_2 sequestration into a fractured aquifer.

To conduct a linear stability analysis, the governing equations of flow and transport given in Eqs. (1)–(4) are linearized. Pressure, velocity, concentration, and density fields are subjected to infinitesimal perturbations as $\mathbf{s} = \mathbf{s}_0 + \mathbf{s}'$ where $\mathbf{s} = \mathbf{s}[p, \mathbf{v}, C, \rho]$; $\mathbf{s}_0$ and $\mathbf{s}'$ are the base state and perturbations, respectively.

Substituting the perturbed variables into the flow and transport equations, implementing the base-state quantities, taking the curl of Eq. (3), and, after simplification, we obtain the following perturbed equations.

$$\frac{\partial^2 C'_f}{\partial z^2} - w' \frac{\partial C_{0f}}{\partial z} = \frac{\partial C'_f}{\partial t}, \tag{16}$$

$$\frac{\partial^2 C'_m}{\partial \ell^2} = \frac{1}{\lambda} \frac{\partial C'_m}{\partial t}, \tag{17}$$

$$\nabla^2 w' = \mathrm{Ra} \nabla^2 C'_f, \tag{18}$$

where the velocity perturbation is scaled by $(\phi D)_f / H$, $\nabla^2 = \nabla^2_{xy}$, $\mathrm{Ra} = k g \beta C^* H / \mu (\phi D)_f$ is the Rayleigh number, and the

hats (^) are dropped for convenience. w' denotes the vertical component of the Darcy velocity perturbation, and C^* is the equilibrium concentration (maximum concentration) of the diffusing species in the aqueous phase.

By using the Fourier decomposition method, the perturbed velocity and concentration are expressed as

$$[C'_f, C'_m, w'] = [C_f^*, C_m^*, w^*](z, t_0) e^{-i \kappa x + \sigma t}, \tag{19}$$

where κ and σ are the perturbation wave number and growth rate, respectively. Using Eq. (19) the decomposed perturbed equations can be written as

$$\frac{d^2 C_f^*}{dz^2} - \kappa^2 C_f^* - w^* \frac{\partial C_{0f}}{\partial z} = (\sigma) C_f^*, \tag{20}$$

$$\frac{d^2 w^*}{dz^2} - \kappa^2 w^* = \mathrm{Ra}(-\kappa^2) C_f^*, \tag{21}$$

with the boundary conditions $w^*(z = 0) = w^*(z = 1) = 0$, $C^*(z = 0) = 0$, and $\partial C^*(z = 1)/\partial z = 0$.

To find the growth rate σ as a function of wave number κ, Eqs. (20) and (21) are solved numerically using the finite difference method. The following eigenvalue problem can be obtained using the discretized perturbed equations (20)
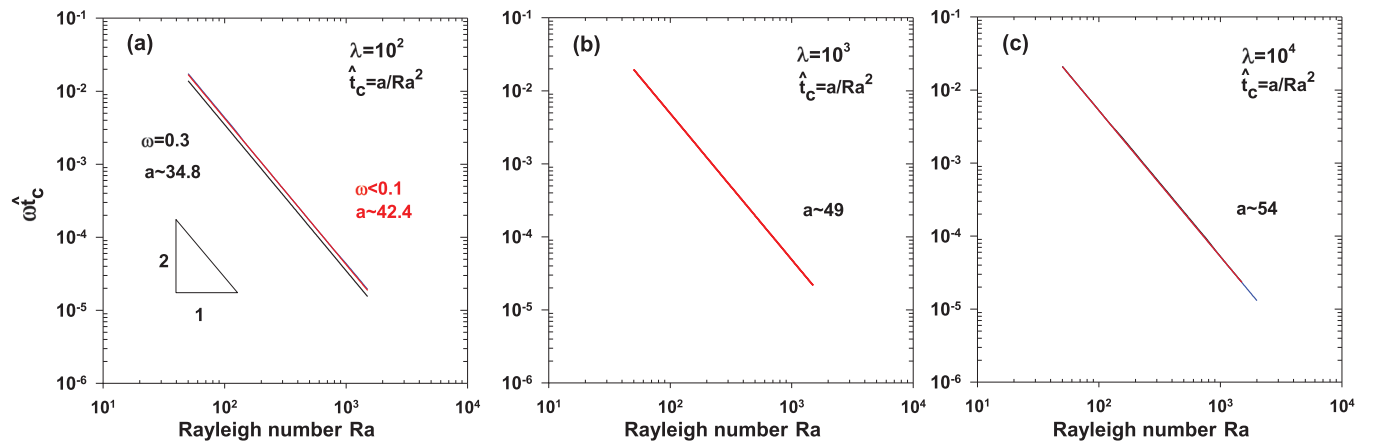

FIG. 6. Onset of instability scaled with Ra for fractured systems with single-size matrix blocks at different fracture interporosity flow coefficients.
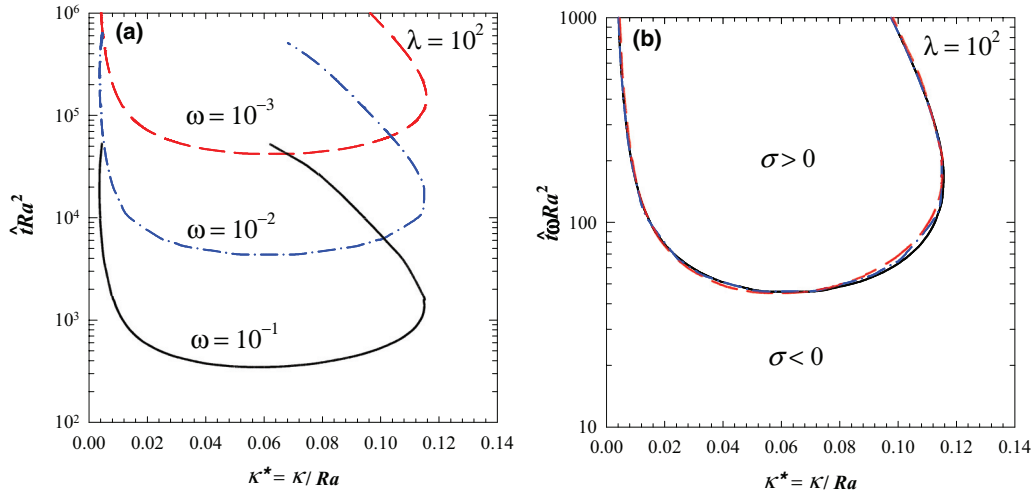
FIG. 7. Neutral stability curves for fractured systems with single-size matrix blocks and a constant fracture interporosity flow coefficient $\lambda = 100$, at different fracture storativity coefficients.

and (21).

$$\left\{ \mathbf{A}_c - \mathrm{Ra}(-\kappa^2)\mathbf{A}_w^{-1}\frac{\partial C_{0f}}{\partial z} \right\}[C^*] = [\sigma][C^*], \qquad (22)$$

where $\mathbf{A}_w = (\mathbf{D}_w - \kappa^2\mathbf{I})$, $\mathbf{A}_c = (\mathbf{D}_c - \kappa^2\mathbf{I})$; $\mathbf{D}_w$ and $\mathbf{D}_c$ are coefficient matrices based on central discretization of the second derivatives and c and w are subscripts for concentration and velocity, respectively.

The above eigenvalue problem is solved numerically for a range of system physical properties at a certain diffusive time. The same numerical procedure addressed in the previous studies [54] is employed to solve the eigenvalue problem. The maximum eigenvalue of the coefficient matrix is considered as the growth rate σ, corresponding to the assigned wave number κ, and Ra at a certain time. The time at which the growth rate turns positive at the given Ra number represents the onset of instability.

V. RESULTS AND DISCUSSION

Linear stability analysis was conducted to study the effect of the physical properties of fractured porous media and interaction of matrix and fracture on the onset of density-driven convection. In the following, the stability criterion of the diffusive boundary layer in a fractured porous medium is examined for a wide range of dual porosity parameters.

Figure 4 shows the growth rate of perturbations for a system with different fracture storativity and interporosity flow coefficients at a constant Ra number and $\hat{t}_0 = 18 \times 10^{-3}$. Linear stability analysis results reveal different growth rates for these systems, suggesting different instability behavior. Results of perturbation growth rates for systems with a constant interporosity flow coefficient λ, shown in Fig. 4(a), indicate that systems with larger fracture storativity ω lead to higher perturbation growth rates. This may imply that systems with larger fracture storativity are gravitationally less stable than those with smaller ω.

Results of growth rates for systems with a constant fracture storativity and Ra number are shown in Fig. 4(b) for different interporosity flow coefficients. It can be observed that increase

of interporosity flow coefficient leads to lower perturbations growth rates, suggesting a more stable diffusive boundary layer. In other words, the fracture to matrix mass transfer has a stabilizing effect. To further clarify these findings, results of onset of the convective instabilities versus Ra for various fracture storativity and interporosity flow properties are shown in Fig. 5.

Figure 5 shows the onset of instabilities as a function of Rayleigh number for fractured systems with single-size matrix blocks at different fracture storativity and interporosity flow coefficients. Results show that in all cases the onset time of instability is inversely promotional to the square of the Rayleigh number, implying that the onset time is independent of the porous layer thickness, which is in agreement with previous findings [14,16,65,66]. Results of stability analysis shown in Fig. 5(a) clearly indicate the important role of fracture storativity on the onset of instability. For a given Ra number and fracture interporosity flow coefficient, it is observed that a fractured system with larger fracture storativity shows the
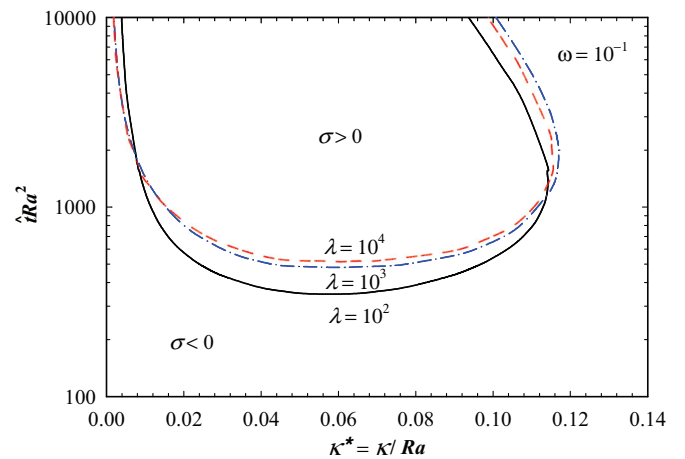

FIG. 8. Neutral stability curves for fractured systems with single-size matrix blocks and a constant fracture storativity $\omega = 0.1$, at different fracture interporosity flow coefficients.
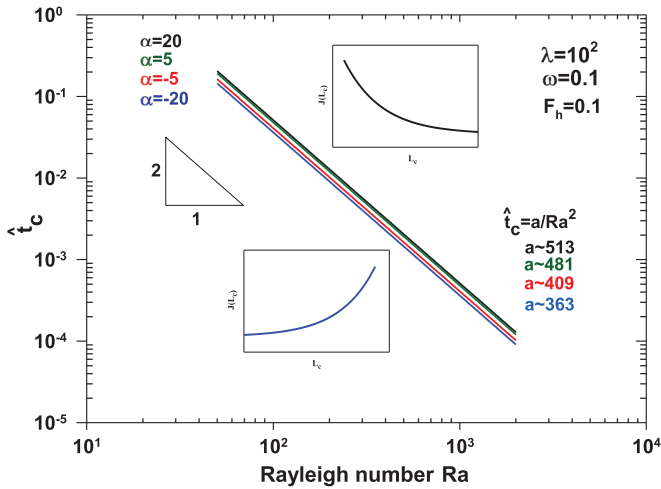
FIG. 9. Onset of instability as a function of Ra number for fractured systems with different matrix block sizes represented by exponential probability density function at constant fracture storativity and interporosity flow coefficients. The inset plots show the matrix block size probability distribution.

earlier onset time. This is in agreement with previous findings for the effect of fracture density and storativity on the onset and dynamics of density-driven flow in fractured porous media [43,44,51]. For the case of a single-porosity system with fracture properties ($\omega = 1$), linear stability analysis results in a scaling prefactor value of $a \sim 56$ for the dimensionless onset time as a function of Ra number. This is in agreement with previous studies [9,15,67,68]. Scaling results also show that the value of prefactor a, representing the onset of density-driven instability at constant Ra and interporosity flow coefficient, significantly increases as the fracture storativity factor decreases. Comparison of scaling onset results for systems with different fracture interporosity flow coefficients also shows that the onset of instability is delayed as the fracture to matrix interporosity flow coefficient increases. This observation is in agreement with those reported in the literature [3,30,31,49,50]. This instability behavior is attributed to the stabilizing effect of fracture to matrix mass transfer

on the growth rate of perturbations in the diffusive boundary layer.

Careful review of the onset time results for a system with constant Ra number and fracture interporosity flow coefficient shows that the rescaling of the onset time as a function of Ra number leads to a single scaling with unique prefactor a/ω for cases with fracture storativity coefficients less than 0.1. It is worth noting that most of the natural fractured systems have fracture storativity below 0.1. The new scaling onset time is shown in Fig. 6.

Figure 7 shows the effect of fracture storativity on the neutral stability curves for fractured systems with a constant interporosity flow coefficient, $\lambda = 100$. The results clearly show that the instability limit in the neutral stability curves significantly shifts upward as fracture storativity decreases. This observation suggests that the system turns more stable at smaller fracture storativities. Rescaling the transient time by multiplying it by the fracture storativity coefficient leads to a single neutral curve suggesting a unified stability limit for a constant interporosity flow coefficient as shown in Fig. 7(b).

The neutral stability curves for the fractured systems with constant fracture storativity $\omega = 0.1$, at different fracture interporosity flow coefficients $\lambda = 100$, 1000, and 10 000, are also shown in Fig. 8. The neutral curves show that as the interporosity flow coefficient increases the system turns more stable. It can be observed that the regions of instability ($\sigma > 0$) move upward as the fracture interporosity flow coefficients increase.

The QSSA formulation of the dual porosity problem does not allow explicit parametric analysis of the stability problem. In Appendix, we use the Galerkin technique [16,21] to convert the linearized perturbation equations [Eqs. (16)–(18)] to a system of ordinary differential equations, which allows analysis of the stability criterion for the special limiting cases of dual porosity parameters (λ and ω).

It is of interest to find out how the variability of matrix block sizes in the fracture aquifers may influence the instability behavior of the diffusive boundary layer. Figure 9 shows the scaling of the onset time as a function of Rayleigh number for fractured systems with different fracture intensities at constant storativity and interporosity flow coefficients. The exponential
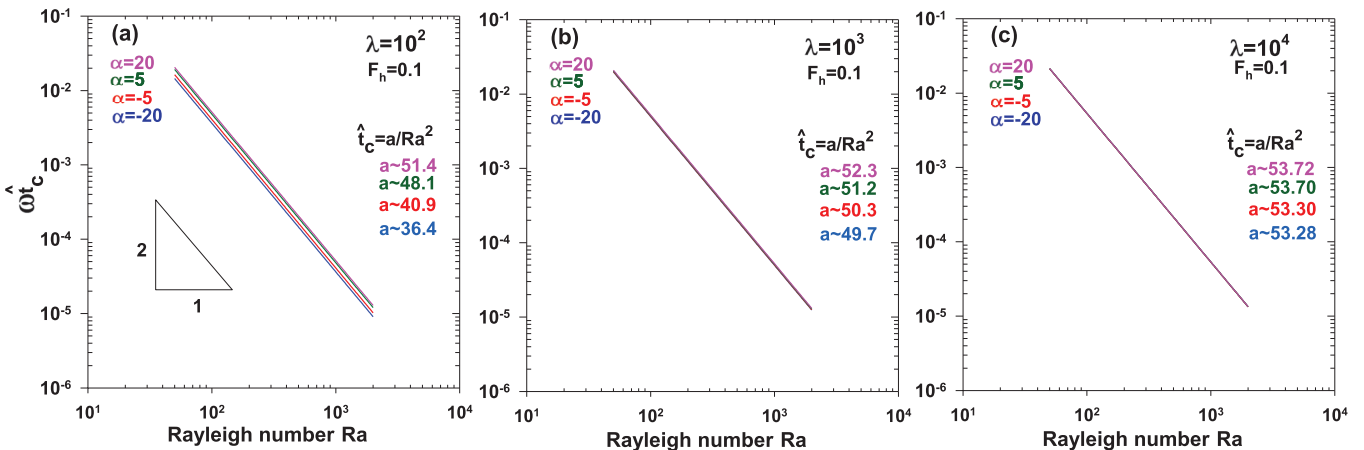

FIG. 10. Scaled onset time of instability for fractured systems with variable matrix block size at different fracture interporosity flow coefficients.

probability density function with four different common values of $\alpha = -20, -5, 5$, and 20 at the constant fracture uniformity $F_h = 0.1$ was employed to represent the matrix block size distribution [69]. For an exponential probability density function [see Eqs. (6) and (10)], positive values of m (α in dimensionless form) imply higher fracture intensity and negative values of m infer sparse fracturing. Scaling results for the onset time versus Ra number show that increase of fracture intensity (positively increasing of α value) stabilizes the diffusive boundary layer leading to higher onset time. This suggests that the diffusive boundary layer for an intensively fractured system is more stable than the sparse one. This instability behavior is expected since for an intensely fractured system mass transfer between matrix and fracture is higher, thus promoting stability of the boundary layer.

Figure 8 shows the scaling of the onset time as a function of Ra number for a fractured system with exponential matrix block size distribution at different fracture storativity and interporosity flow coefficients. It can be observed that the onset time can be rescaled as a unique scaling for systems with fracture storativity coefficients less than 0.1. The results shown in Figs. 10(a)–10(c) also indicate that the impact of matrix block size distribution on the onset of instability decreases as the fracture interporosity flow coefficient increases.

VI. CONCLUSION

We have conducted a linear stability analysis to investigate the onset of natural convection involved in the CO_2 sequestration process in fractured saline aquifers. The dual porosity model was employed to describe the solute transport in fractured media. The effect of physical properties of the fractured porous media on the stability of a transient diffusive boundary was investigated. It was shown that increase of the interporosity flow coefficient leads to a more stable diffusive boundary layer. It was also shown that a diffusive boundary layer under the gravity field in a fractured porous medium with a higher fracture storativity coefficient is less stable. We also examined the effect of matrix block size distribution on the stability behavior of the diffusive boundary layer using an exponential probability density function. It was observed that increase of fracture intensity stabilizes the diffusive boundary layer leading to a delayed onset time. In general, it was shown that the diffusive boundary layer for an intensively fractured system is more stable than the sparse one. Results of the onset time show that the impact of matrix block size distribution on the onset of instability decreases as the fracture interporosity flow coefficient increases. The scaling relation for the onset of convection as a function of Rayleigh number, fracture interporosity and storativity coefficients, and matrix block size distribution properties were developed. It was shown that the onset time as a function of Ra number for cases with fracture storativity coefficients less than 0.1 can be presented using a single scaling relation with unique prefactor a/ω. Such scaling relationships are of great importance in characterization of the fate of the injected CO_2, risk assessment, and site screening purposes.

Finally, we used an idealization of the dual porosity formulation. The behavior of mixing beyond the onset of convection in complex fractured formations in the presence of heterogeneity calls for further studies. The current study paves the way for further studies in this area.

APPENDIX: SEMIANALYTICAL TREATMENT OF THE LINEAR STABILITY FOR SPECIAL CASES

The detailed linear stability analysis in the main text was conducted using the QSSA, which does not allow explicit representation of the special cases. Here, we use the Galerkin technique [16,21], which allows explicit parametric analysis of the stability problem for some limiting cases.

The linearized Eqs. (16)–(18) can be transformed into ordinary differential equations (ODEs) using the Galerkin technique [16,21]. The resulting ODEs can be rearranged to find the Rayleigh numbers as a function of the dual porosity parameters (λ and ω) as given by

$$\mathrm{Ra} = \left\{ \frac{db_l}{d\hat{t}} + \left[\kappa^2 + \left(l - \frac{1}{2}\right)^2 \pi^2 \right] b_l \right\}$$
$$\times \frac{[(l\pi)^2 + \kappa^2](1 - 4l)}{2\kappa^2 l\pi \, b_l \left[\frac{(4l-1)^2}{\eta_{2l} f'_{\eta_{2l}}} e^{\eta_{2l}\hat{t}} + \frac{1}{\eta_1 f'_{\eta_1}} e^{\eta_1 \hat{t}} \right]}, \quad \text{(A1)}$$

where b is the time-dependent amplitude of concentration perturbation fracture in the fracture domain; $l = 1, 2, \ldots, N$ is the summation index in the Fourier expansion of the concentration perturbation; and other parameters have been defined in Sec. III. Equation (A1) allows explicit parametric analysis of the stability problem for special cases as described in the following.

Special cases

Case (i) $\lambda \to \infty$. The relation given for the Rayleigh number in Eq. (A1) reduces to the following equation when $\lambda \to \infty$:

$$\mathrm{Ra} = \left(\frac{\omega + 1}{\omega} \right)$$
$$\times \frac{\pi \left\{ \frac{db_l}{d\hat{t}} + \left[\kappa^2 + \left(l - \frac{1}{2}\right)^2 \pi^2 \right] b_l \right\} [(l\pi)^2 + \kappa^2](4l - 1)}{16\kappa^2 l b_l \left(e^{-\frac{(4l-1)^2 \pi^2}{4}\hat{t}} + e^{-\frac{\pi^2}{4}\hat{t}} \right)}.$$
$$\text{(A2)}$$

This equation indicates that the onset time is independent of λ when $\lambda \to \infty$. The detailed analysis using QSSA also shows that for $\lambda \geqslant 10^4$ the onset time is independent of λ.

Case (ii) $\omega \to 1$. The relation given for Rayleigh number in Eq. (A1) reduces to the following equation

when $\omega \to 1$:

$$\text{Ra} = \frac{\pi \left\{ \frac{db_l}{d\hat{t}} + \left[\kappa^2 + \left(l - \frac{1}{2} \right)^2 \pi^2 \right] b_l \right\} [(l\pi)^2 + \kappa^2](4l - 1)}{8\kappa^2 l b_l \left(e^{-\frac{(4l-1)^2 \pi^2}{4} \hat{t}} + e^{-\frac{\pi^2}{4} \hat{t}} \right)},$$

$$(A3)$$

which is equivalent to Case i ($\lambda \to \infty$) when $\omega = 1$.

Case (iii) $\omega \to 0$. The relation given for the Rayleigh number in Eq. (A1) reduces to Ra $= \infty$ when $\omega \to 0$, which indicates an unconditionally stable state. It is worth noting that this conclusion has been reached as a result of the dual porosity assumption where the transport mechanism in the matrix is pure diffusion.

Case (iv). When $\tanh \sqrt{\eta_n/\lambda} \approx 1$ or $\sqrt{\eta_n/\lambda} \geqslant 4$ it can be shown that

$$\text{Ra} = \frac{\pi}{4\kappa^2 l b_l g_l} \left\{ \frac{db_l}{d\hat{t}} + \left[\kappa^2 + \left(l - \frac{1}{2} \right)^2 \pi^2 \right] b_l \right\}$$

$$\times [(l\pi)^2 + \kappa^2](4l - 1),$$

where g_l is only a function of $(1 - \omega)\sqrt{\lambda}/\omega$, $\hat{t}$. This indicates that for a constant Ra, the onset time is only a function of κ and $(1 - \omega)\sqrt{\lambda}/\omega$. In other words, $t_c = \wp(\text{Ra}, \kappa, (1 - \omega)\sqrt{\lambda}/\omega)$.

Case (v). $\lambda \to 0$ while $\omega > 0$: The relation given for the Rayleigh number in Eq. (A1) reduces to Eq. (A3) in this case.

---

[1] E. Lindeberg and D. Wessel-Berg, Energy Convers. Manage. **38**, S229 (1997).

[2] J. Carballido-Landeira, P. M. J. Trevelyan, C. Almarcha, and A. De Wit, Phys. Fluids **25**, 024107 (2013).

[3] P. Alt-Epping and B. C. Zhao, J. Geochem. Explor. **106**, 8 (2010).

[4] C. Zhao, B. E. Hobbs, and A. Ord, *Fundamentals of Computational Geoscience: Numerical Methods and Algorithms* (Springer, Berlin, 2009).

[5] D. A. Nield and A. Bejan, *Convection in Porous Media* (Springer Science & Business Media, New York, 2006).

[6] H.-J. G. Diersch and O. Kolditz, Adv. Water Resour. **25**, 899 (2002).

[7] C. Zhao, B. E. Hobbs, and A. Ord, *Convective and Advective Heat Transfer in Geological Systems* (Springer, Berlin, 2008).

[8] P. M. J. Trevelyan, C. Almarcha, and A. De Wit, J. Fluid Mech. **670**, 38 (2011).

[9] S. M. Jafari Raad and H. Hassanzadeh, Phys. Rev. E **92**, 053023 (2015).

[10] V. Loodts, C. Thomas, L. Rongy, and A. De Wit, Phys. Rev. Lett. **113**, 114501 (2014).

[11] K. S. Lackner, Science **300**, 1677 (2003).

[12] J. P. Ennis-King and L. Paterson, SPE J. **10**, 349 (2005).

[13] H. Hassanzadeh, M. Pooladi-Darvish, and D. W. Keith, J. Can. Pet. Technol. **44**, 43 (2005).

[14] J. Ennis-King, I. Preston, and L. Paterson, Phys. Fluids **17**, 084107 (2005).

[15] A. Riaz, M. Hesse, H. A. Tchelepi, and F. M. Orr, J. Fluid Mech. **548**, 87 (2006).

[16] H. Hassanzadeh, M. Pooladi-Darvish, and D. W. Keith, Transp. Porous Media **65**, 193 (2006).

[17] A. C. Slim and T. S. Ramakrishnan, Phys. Fluids **22**, 124103 (2010).

[18] J. S. Hong and M. C. Kim, Transp. Porous Media **72**, 241 (2008).

[19] S. Rapaka, R. J. Pawar, P. H. Stauffer, D. Zhang, and S. Chen, J. Fluid Mech. **641**, 227 (2009).

[20] S. Rapaka, S. Chen, R. J. Pawar, P. H. Stauffer, and D. Zhang, J. Fluid Mech. **609**, 285 (2008).

[21] X. Xu, S. Chen, and D. Zhang, Adv. Water Resour. **29**, 397 (2006).

[22] J. T. H. Andres and S. S. S. Cardoso, Phys. Rev. E **83**, 046312 (2011).

[23] H. Hassanzadeh, M. Pooladi-Darvish, and D. W. Keith, AIChE J. **53**, 1121 (2007).

[24] G. S. H. Pau, J. B. Bell, K. Pruess, A. S. Almgren, M. J. Lijewski, and K. Zhang, Adv. Water Resour. **33**, 443 (2010).

[25] J. J. Hidalgo, C. W. MacMinn, and R. Juanes, Adv. Water Resour. **62**, 511 (2013).

[26] C. Chen and D. Zhang, Water Resour. Res. **46**, 1 (2010).

[27] A. Zebib and D. R. Kassoy, Phys. Fluids **20**, 4 (1977).

[28] D. R. Kassoy and B. Cotte, J. Fluid Mech. **152**, 361 (1985).

[29] C. Zhao, B. E. Hobbs, A. Ord, S. Peng, H. B. Mühlhaus, and L. Liu, Math. Geol. **37**, 373 (2005).

[30] V. I. Malkovsky and A. A. Pek, Phys. Solid Earth **40**, 672 (2004).

[31] H. D. Murphy, J. Geophys. Res. **84**, 6121 (1979).

[32] P. D. Weidman and D. R. Kassoy, Phys. Fluids **29**, 349 (1986).

[33] T. Graf and R. Therrien, Adv. Water Resour. **31**, 1352 (2008).

[34] C. Zhao, B. E. Hobbs, A. Ord, S. Peng, H. B. Mühlhaus, and L. Liu, Tectonophysics **387**, 47 (2004).

[35] V. I. Malkovsky and F. Magri, Water Resour. Res. **52**, 2855 (2016).

[36] J. Yang, K. Latychev, and R. N. Edwards, Geophys. J. Int. **135**, 627 (1998).

[37] D. W. Peaceman, Soc. Pet. Eng. J. **16**, 269 (1976).

[38] D. W. Peaceman, Soc. Pet. Eng. J. **16**, 281 (1976).

[39] D. W. Ruth, Soc. Pet. Eng. J., 1 (1979).

[40] S. G. Shikaze, E. Sudicky, and F. Schwartz, J. Contam. Hydrol. **34**, 273 (1998).

[41] C. T. Simmons, J. M. Sharp Jr., and D. A. Nield, Water Resour. Res. **44**, W03431 (2008).

[42] K. Vujević and T. Graf, Adv. Water Resour. **84**, 52 (2015).

[43] T. Graf and R. Therrien, Adv. Water Resour. **30**, 455 (2007).

[44] K. Vujević, T. Graf, C. T. Simmons, and A. D. Werner, Adv. Water Resour. **71**, 65 (2014).

[45] J. Yang, Can. J. Earth Sci. **43**, 1331 (2006).

[46] A. M. Saidi, *Reservoir Engineering of Fractured Reservoirs: Fundamental and Practical Aspects* (Total Edition Press, Paris, 1987).

[47] S. H. Davis, J. Fluid Mech. **30**, 465 (1967).

[48] D. A. Nield, Water Resour. Res. **4**, 553 (1968).

[49] C. Zhao, B. E. Hobbs, A. Ord, M. Kühn, H. B. Mühlhaus, and S. Peng, Comput. Methods Appl. Mech. Eng. **195**, 2816 (2006).

[50] T. Graf and R. Therrien, Geofluids **9**, 138 (2009).

[51] C. Mezon, V. V. Mourzenko, J.-F. Thovert, R. Antoine, F. Fontaine, A. Finizola, and P. M. Adler, Phys. Rev. E **97**, 013106 (2018).

[52] C. T. Tan and G. M. Homsy, Phys. Fluids **29**, 3549 (1986).

[53] P. M. J. Trevelyan, C. Almarcha, and A. De Wit, Phys. Rev. E **91**, 023001 (2015).

[54] H. Emami Meybodi and H. Hassanzadeh, Phys. Rev. E **87**, 033009 (2013).

[55] G. Barenblatt, I. Zheltov, and I. Kochina, J. Appl. Math. Mech. **24**, 1286 (1960).

[56] J. E. Warren and P. J. Root, Soc. Pet. Eng. J. **3**, 245 (1963).

[57] A. S. Odeh, Soc. Pet. Eng. J. **5**, 60 (1965).

[58] Q. Zhou, C. M. Oldenburg, L. H. Spangler, and J. T. Birkholzer, Water Resour. Res. **53**, 1746 (2017).

[59] R. T. Johns and Y. Jalali, SPE Form. Eval. **6**, 513 (1991).

[60] P. Segall, The development of joints and faults in granitic rocks, Ph.D. thesis, Stanford University, 1981.

[61] T. A. Jelmert, J. Pet. Sci. Eng. **12**, 277 (1995).

[62] R. W. Zimmerman and G. S. Bodvarsson, Geophys. Res. Lett. **22**, 1461 (1995).

[63] E. Ranjbar, H. Hassanzadeh, and Z. Chen, Transp. Porous Media **95**, 185 (2012).

[64] H. S. Carslaw and J. C. Jaeger, *Conduction of Heat in Solids* (Clarendon Press, Oxford, 1959).

[65] A. C. Slim, J. Fluid Mech. **741**, 461 (2014).

[66] B. Meulenbroek, R. Farajzadeh, and H. Bruining, Phys. Fluids **25**, 074103 (2013).

[67] S. M. Jafari Raad and H. Hassanzadeh, Int. J. Greenhouse Gas Control **54**, 250 (2016).

[68] S. M. Jafari Raad, H. Emami-Meybodi, and H. Hassanzadeh, Water Resour. Res. **52**, 4458 (2016).

[69] R. Rodriguez-N., H. Cinco-L., and F. Samaniego-V., in *Proceedings of the SPE Annual Technical Conference and Exhibition, 2001 New Orleans* (Society of Petroleum Engineers, Richardson, TX, 2001).